An Active Alkali-Exchanged Faujasite Catalyst for *p*-Xylene Production via the One-Pot Diels−Alder Cycloaddition/Dehydration Reaction of 2,5-Dimethylfuran with Ethylene

Roderigh Y. Rohling,[†] Evgeny Uslamin,[†] Bart Zijlstra,[†] Ionut C. Tranca,[†,§] Ivo A. W. Filot,[†] Emiel J. M. Hensen,*[†] and Evgeny A. Pidko*[†,‡,‖]

[†]Inorganic Materials Chemistry group, Department of Chemical Engineering, Eindhoven University of Technology, P.O. Box 513, 5600 MB Eindhoven, The Netherlands

[‡]TheoMAT group, ITMO University, Lomonosova Street 9, St. Petersburg 191002, Russia

S *Supporting Information*

ABSTRACT: The one-pot Diels−Alder cycloaddition (DAC)/dehydration (D) tandem reaction between 2,5-dimethylfuran and ethylene is a potent pathway toward biomass-derived *p*-xylene. In this work, we present a cheap and active low-silica potassium-exchanged faujasite (KY, Si/Al = 2.6) catalyst. Catalyst optimization was guided by a computational study of the DAC/D reaction mechanism over different alkali-exchanged faujasites using periodic density functional theory calculations complemented by microkinetic modeling. Two types of faujasite models were compared, i.e., a high-silica alkali-exchanged faujasite model representing isolated active cation sites and a low-silica alkali-exchanged faujasite in which the reaction involves several cations in the proximity. The mechanistic study points to a significant synergetic cooperative effect of the ensemble of cations in the faujasite supercage on the DAC/D reaction. Alignment of the reactants by their interactions with the cationic sites and stabilization of reaction intermediates contribute to the high catalytic performance. Experiments confirmed the prediction that KY is the most active catalyst among low-silica alkali-exchanged faujasites. This work is an example of how the catalytic reactivity of zeolites depends on multiple interactions between the zeolite and reagents.

KEYWORDS: Diels−Alder, DFT calculations, confinement effects, biomass, structure−activity relations
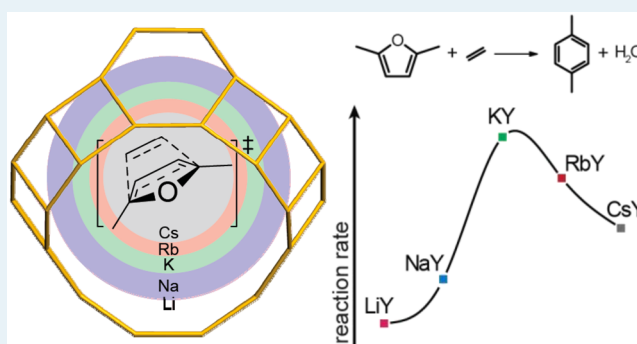
1. INTRODUCTION

Zeolites make up an important class of inorganic materials with major applications in heterogeneous catalysis. They are crystalline microporous aluminosilicates. The molecule-sized micropores are arranged in different manners, giving rise to >200 different pore topologies. During zeolite catalysis, reactivity is controlled by the intrinsic properties of the active sites, either protons or Lewis acid sites, and the shape selectivity induced by the confined space around the active sites.[1−3]

Zeolites are traditionally used in refinery processes. More recently, the use of zeolites in the context of valorization of biomass into chemicals and fuels has also been explored.[4−6] Lewis acid zeolite catalysts can play an important part in upgrading renewable lignocellulosic biomass feedstock toward highly valuable aromatic products, which are currently produced solely from fossil hydrocarbon resources.[7,8] Most desired aromatics are toluene and xylenes. Among the different xylene isomers, the market demand for *p*-xylene is the highest.[9]

The primary constituents of biomass are cellulose, hemicellulose, and lignin.[10] Of the former two, cellulose is a crystalline linear polysaccharide built from glucose, and

hemicellulose is an amorphous polysaccharide whose major constituent is xylose. Lignin, on the other hand, is a large polyaromatic polymer. Both the polysaccharide- and polyaromatic-based compounds require significant upgrades before aromatic compounds are obtained. One of the possible pathways for obtaining aromatic compounds from (hemi)-cellulose starts with hydrolysis followed by isomerization and stepwise hydrogenation of the released monosaccharides (i.e., glucose in the case of cellulose), yielding various furanic compounds like 5-hydroxymethylfurfural and 2,5-dimethylfuran (Figure 1a).[11−13] These furanic compounds are considered biomass platform molecules, and their conversion to industrially important intermediates is a challenging task. One approach to obtaining aromatics from furanics is the sequential Diels−Alder cycloaddition (DAC) and dehydration (D) with alkenes (DAC/D reaction).[14−16] After the DAC reaction, the 7-oxanorbornene cycloadduct is dehydrated to obtain the final
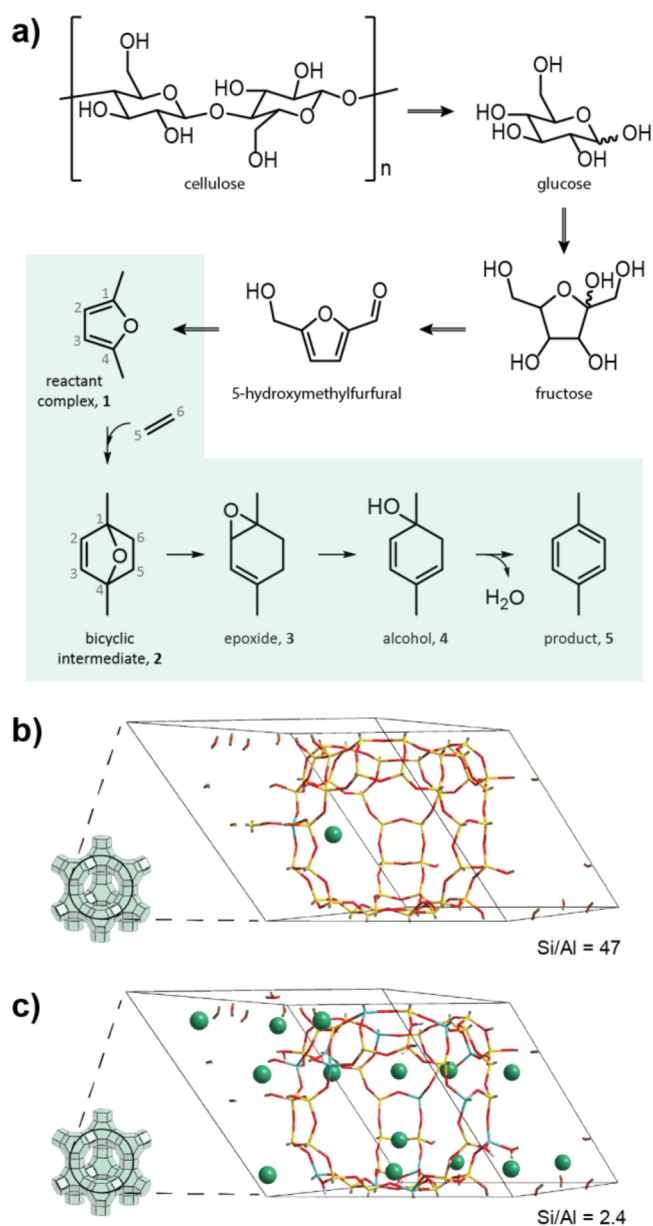
Figure 1. (a) Schematic representation of the biomass-derived aromatic production route starting from cellulose with the reaction of interest for this study highlighted with the green background. (b) Periodic high-silica faujasite model used in this work. (c) Periodic low-silica faujasite model with a chemical composition matching that of the as-synthesized catalyst.

aromatic product.[17,18] Lewis acid (LA) zeolites are potential catalysts for such reactions, as (i) the DAC reaction is a textbook example of an organic reaction greatly benefiting from LA catalysis and (ii) catalyst separation from the product stream is far easier with heterogeneous catalysts than with homogeneous catalysts.[16,19] Moreover, Lewis acids catalyze fewer undesirable side reactions in biomass upgrading than Brønsted acid (BA) zeolites do.[20]

A range of catalysts have been investigated to enhance the DAC/D reaction of DMF with ethylene,[21−28] as part of a wider search for DAC/D-based production pathways toward aromatic compounds with different furanic or alkene reactants.[29−34] Examples of heterogeneous catalysts for *p*-xylene from furanics include HY,[21−24] HBEA,[25] MBEA (M = Sn, Ti, or Zr),[26,27] and

silica−alumina aerogels.[28] Among these studies, Vlachos and co-workers compared the one-pot DAC/D reaction of DMF with ethylene over HY and alkali-exchanged faujasites.[21,22] In their work, the mechanistic picture was derived from models such as an isolated cation[22] or a larger ONIOM cluster model.[21] The reaction energetics of Brønsted and Lewis acid sites in zeolites were compared. A conclusion of this work was that the NaY-catalyzed reaction is limited by the dehydration of the bicyclic intermediate.[21]

With respect to these important initial studies, we can ask whether a single-cation model of the active sites in alkali-exchanged faujasite can capture all the relevant features. This is related to the nature of the active site, e.g., the local active site topology, the density of the active site, and the active site chemical composition. Often, catalysts are studied via a reductionist approach in which the chemical complexity of the catalytic system is simplified. It is becoming clearer that such a reductionist approach alone is not sufficient to understand the activity of catalysts whose reactivity depends on their complex chemical composition.[35] For instance, heterogeneous surface reactions are often profoundly affected by nearby active sites and adsorbates occupying these sites.[36−38] During homogeneous catalysis, the participation of the solvent has been shown to play an important role in influencing the reaction energetics and reaction pathway.[39,40] In enzymatic[41,42] and zeolite[43,44] catalysis, it is becoming increasingly evident that the surrounding matrix and the nearby active groups or sites within the catalytic pocket or zeolite pore play an immense role in the reaction energetics. Taking these aspects into account is important if one aims to predict catalytic performance.

In this work, we employ periodic density functional theory (DFT) calculations and microkinetic modeling to reveal the role of reactant confinement on the DAC/D reaction of DMF with ethylene to *p*-xylene as a model reaction. The key focus is on establishing the key parameters that control the reactivity of Lewis acid zeolite catalysts in the DAC/D reactions beyond the isolated site model. To this end, we used periodic high- and low-silica alkali-exchanged faujasite zeolite models. This allowed us to study the reactivity for the conventional isolated site model (high-silica zeolite) as well as low-silica models capturing the higher complexity of the actual catalyst systems containing multiple accessible sites. The computational results indicate that a high density of accessible sites near the reactants and reaction intermediates in the zeolite micropore are important factors that determine the catalytic performance. Our results show that reaction barriers are significantly lowered. Moreover, we find that the reactivity trend among the low-silica alkali-exchanged faujasites is different from the one derived for their high-silica counterparts. On the basis of these results, we predict that potassium should be the most suitable alkali cation for modifying low-silica faujasite to achieve good performance in the DAC/D reaction of DMF with C_2H_4 to obtain *p*-xylene. Alkali-exchanged faujasite catalysts with a chemical composition similar to that of the modeled low-silica faujasites were synthesized and subjected to kinetic tests to experimentally determine the activity trend. The experimental results confirm the theoretical predictions.

2. COMPUTATIONAL AND EXPERIMENTAL DETAILS

Models and Methods. The models were based on the rhombohedral unit cell of faujasite containing 48 T sites and 96 oxygen atoms. The high-silica model (Si/Al = 47; $Si_{47}Al_1O_{96}M_1$) contained one isolated site per rhombohedral

unit cell (Figure 1b). The low-silica model (Si/Al = 2.4; $Si_{34}Al_{14}O_{96}M_{14}$) had a high active site density (Figure 1c). M^+ was either Li^+, Na^+, K^+, Rb^+, or Cs^+. More information about the cation placement and lattice relaxations can be found in the Supporting Information. In the following, we will use MFAU to refer to the faujasite model with a Si/Al ratio of 47 and MY to refer to the model with a Si/Al ratio of 2.4. The starting geometries were selected on the basis of geometric considerations combined with a preliminary computational screening of a range of alternative adsorption modes. The computed adsorption energies for the different optimized adsorption complexes are summarized in Tables S1 and S2.

All periodic DFT calculations were performed with the gradient-corrected PBE exchange-correlation functionals implemented in the Vienna Ab-Initio Simulation Package (VASP).[45−49] The projected-augmented-wave scheme (PAW) was used to describe the electron−ion interactions. Long-range dispersive interactions were accounted for by using the DFT-D3 method with Becke−Johnson damping.[50,51] The k-point mesh was reduced to the Γ point. The cutoff energy for the plane-wave basis set was 500 eV, and a root-mean-square (RMS) force convergence criterion of 0.015 eV/Å was employed. Occasionally, some models did not fully reach this strict RMS force criterion, and the convergence criterion was relaxed to 0.035 eV/ Å. This was caused by strong forces on cations confined within the double six rings distant from the active site. The relaxed convergence criteria were deemed acceptable because the current zeolite models feature extremely shallow potential energy surfaces. Structural optimization below 0.05 eV/Å usually led to energy changes of <5 kJ/mol.

To identify the transition state, a two-step approach was adopted. First, a Climbing-Nudged-Elastic Band (CNEB) calculation[52,53] was performed to estimate the minimum energy pathway (MEP) (spring constant of 5 eV/Å², maximum length hypervector between images of 0.5 Å). The accepted RMS force of the converged CNEB was ≤0.14 eV/Å. Next, the geometry of the identified transition state was further optimized using the quasi-newton procedure (maximum RMS of <0.015 eV/Å). Vibrational frequencies were then calculated with the finite displacement method (0.0015 Å) to confirm the nature of the stationary point.

Microkinetic Modeling. The reaction energy diagrams derived from the DFT calculations were used to compute rate constants for a microkinetic model of the DAC/D reaction. The set of reaction equations used in the MKM modeling efforts is shown in Table S3. The calculations were performed with a C++ program written in house.[54,55]

For N elementary reactions, we can define $2N$ elementary reaction steps, i.e., both forward and backward:

$$r_n = k_n \prod_i c_i^{\nu_{i,n}} \tag{1}$$

where c_i is the concentration of reactant i in elementary reaction step n. In the rate equation, ν_i is the stoichiometric coefficient of species i in reaction n. The time-dependent concentration of component i is

$$\frac{dc_i}{dt} = \sum_n v_{i,n} r_n \tag{2}$$

Furthermore, we considered competitive adsorption of the reactants, followed by surface reactions toward the products that then desorb again. Re-adsorption of the products was not taken into account; i.e., the simulation was performed in the low-conversion limit. This yields for adsorption

$$r_{R,ads} = k_{R,ads} C_R \theta_* \tag{3}$$

where R is the concentration of either DMF or C_2H_4 and θ the fraction of available free sites. Desorption is described as

$$r_{P*,des} = k_{P*,des} C_{P*} \tag{4}$$

where C_P* is that for either of the two reactants (DMF and C_2H_4) or the two products (p-xylene and H_2O).

The rate constants of the individual elementary reaction steps are determined using the Eyring equation:[56]

$$k_n = A_n \exp\left(\frac{-\Delta E_n^{\ddagger}}{k_b T}\right) \tag{5}$$

with

$$A_n = \left(\frac{k_b T}{h}\right)\left(\frac{Q_n^{\ddagger}}{Q_n^{IS}}\right) \tag{6}$$

where for elementary reaction step n the DFT-computed activation energy is denoted as $E^{\ddagger}$ and $Q^{\ddagger}$ and Q^{IS} are the partition functions of the corresponding initial and transition state, respectively. The ratio of the partition functions defines the activation entropy, as

$$\left(\frac{Q_n^{\ddagger}}{Q_n^{IS}}\right) = \exp\left(\frac{\Delta S_n^{\ddagger}}{k_b}\right) \tag{7}$$

We then assumed all elementary reactions to take place with both equal probability and no significant entropy change (mainly vibrational in the adsorbed state). Therefore, the exponential prefactor is $A_{react.} = [(k_b T)/h] \approx 10^{13}$. Because most of the entropy losses are encountered during the adsorption step, the value of 10^{13} is a reasonable approximation of the pre-exponential factors for the reactions occurring over active surface sites within the harmonic limit.[57] Additionally, we assumed mobile transition states for product desorption, so that $A_{des.} = 10^{15}$. Furthermore, we varied the adsorption prefactors of the reactants (A_{DMF} and $A_{C_2H_4}$), reflecting differences in pressure. Note that the molecular adsorption rate constant for reactant i can be described as

$$k_{ads,i} = A_{ads,i} = \frac{P_i O}{\sqrt{2\pi M_{w,i} k_b T}} S_i \tag{8}$$

where P_i is the partial pressure (pascals) of the reactant in the gas phase, O the surface area of the adsorption site (square meters), $M_{w,i}$ the reactant mass (kilograms), and S_i the dimensionless sticking number. Let us consider DMF adsorption, for instance, at 10^5 Pa of DMF and 503 K with an O of 1×10^{-20} m² and S_i set to 1. The resulting k_{ads} is 1.4×10^7 s⁻¹.

Next, the degree of rate control (DRC) for every elementary step was determined.[58] Briefly, the DRC for elementary reaction n is defined as the relative change in the overall rate as a function of the changing reaction constant (k_n) while the equilibrium constant remains fixed. This resembles changing the stability of the transition state (TS_n) corresponding to elementary reaction n.
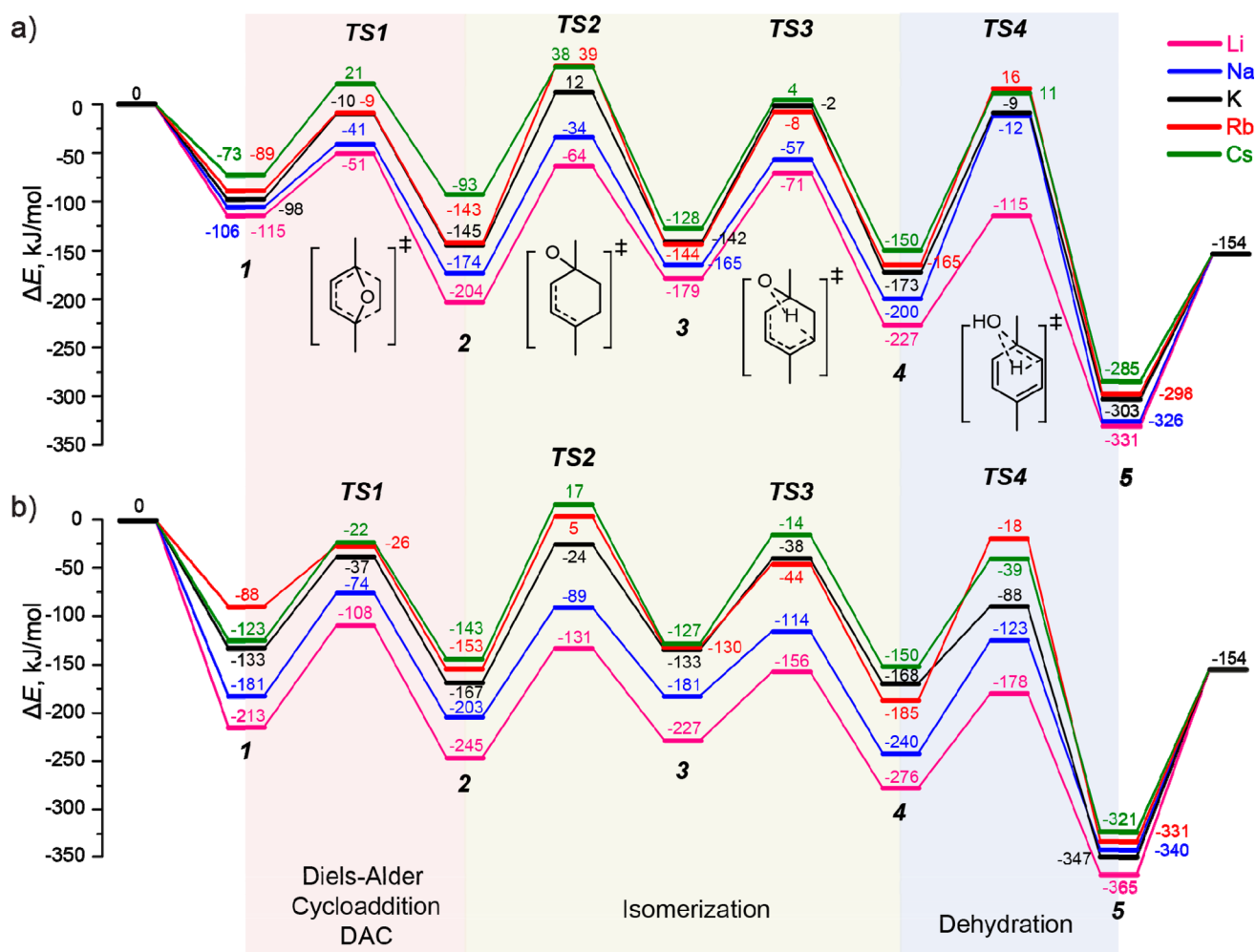
Figure 2. DFT-computed reaction energy diagrams for DAC/D conversion of DMF and ethylene over alkali-exchanged (a) single-site FAU (Si/Al = 47) and (b) realistic Y zeolite (Si/Al = 2.4) models.

$$\chi_{px,n} = \left[\frac{\partial \ln(r_{px})}{\partial \ln(k_n)} \right]_{k_{m \neq n}, K_n} \tag{9}$$

where $\chi_{px,n}$ is the DRC parameter for elementary reaction n for the product p-xylene (px), r_{px} is the overall reaction rate, and k_n and K_n are the forward rate and equilibrium constants for reaction n, respectively. The value for $\chi_{px,n}$ can either be positive or negative, indicating that a step is rate-controlling (increase in rate with a decrease in E_{TS_n}) or rate-inhibiting (decrease in rate with a decrease in E_{TS_n}), respectively. The total sum of all DRCs is always unity.

Catalyst Preparation and Characterization. The parent material NaY (Si/Al = 2.5) was obtained from Akzo Nobel. Aqueous MNO_3 solutions (M = Li, K, Rb, or Cs) were used for ion exchange to obtain the Li, K, Rb, or Cs form of the Y zeolite, respectively. Ion exchange was repeated five times at 343 K for 2 h with 0.5 M MNO_3 solutions using a solution to zeolite ratio of 20 mL/g. After being washed and dried overnight at 383 K, zeolites were calcined at 723 K for 3 h in air. Relevant characterization data of the zeolites are provided in the Supporting Information. The results indicate a high level of cation exchange while crystallinity and porosity are retained.

Reaction Rates. Activity tests were performed in a 100 mL TOP Industrie autoclave equipped with a mechanical stirrer

and a pressure control system. In a typical experiment, catalysts were dried under vacuum at 473 K for 3 h prior to the reaction inside the reactor. The system was heated to the reaction temperature (503 K), and then a 0.5 M solution of DMF in n-heptane was added. When the desired temperature was reached, the reactor was pressurized with 6×10^6 Pa of ethylene. Sampling of the liquid phase was performed every 5–10 min after the start of the reaction. Identification and quantitative analysis of the reaction products were performed using GC-MS and GC-FID systems (Shimadzu GC-MS GC-17A-QP-5050, Stabilwax; Shimadzu GC GC-17A, Rxi-5 ms). To obtain the reaction orders, the reaction rates were measured by varying the initial DMF concentration from 0.3 to 1.5 M.

3. RESULTS AND DISCUSSION

DFT Calculations. *Reaction Mechanism.* The DFT-computed reaction energy diagrams for the DAC/D reaction of DMF with ethylene to p-xylene over different alkali-exchanged faujasites are shown in panels a and b of Figure 2. The one-pot DAC/D reaction starts with the adsorption of the reactants in the supercage (DMF + C_2H_4 + Z → **1**/Z, where Z refers to MFAU or MY). Adsorption is followed by the DAC reaction (**1** → **2**), yielding a bicyclic intermediate (**2**, 1,4-dimethyl-7-oxabicyclo[2.2.1]hept-2-ene). Next, migration of the furanic oxygen (O_f) to a position bridging the C_1/C_2 pair

isomerizes **2** into epoxide **3** (3,6-dimethyl-7-oxabicyclo[4.1.0]-hept-2-ene intermediate). This species isomerizes (**3 → 4**) into an alcohol **4** (1,4-dimethylcyclohexa-2,4-dien-1-ol) via an intramolecular proton transfer from the C_5-methylene group to O_f. The driving force for this reaction is the formation of the conjugated diene and the release of the strain within the epoxide ring. Finally, alcohol **4** is dehydrated (**4 → 5**) via a proton transfer from the C_6-methylene group to O_fH, producing adsorbed *p*-xylene and water (**5** + H_2O). Desorption of these products completes the catalytic cycle.

For the all-silica FAU and MFAU models, independent of M, the adsorption of DMF is almost 2 times stronger than that of ethylene. Adsorption in the former model arises from solely dispersive interactions (Table S1). The adsorption complexes are of the η^5-coordination type between the π-system of DMF and the exchangeable alkali cation. The co-adsorbed state, in which such a coordinated DMF complex shares the confined space of the faujasite supercage with physisorbed ethylene, is the starting point of the catalytic process (**1**/FAU). The individual DMF adsorption and co-adsorption energies (Figure 2a, **1**) for different MFAU models correlate well with the Lewis acidity of the exchangeable cations: the interaction energy decreases with an increase in ionic radius from Li^+ to Cs^+. The co-adsorbed reactants undergo a DAC reaction (**1 → 2**) during which two new bonds are formed synchronously between the C_1–C_6 and C_4–C_5 pairs. The overall reaction enthalpy for the **1 → 2** reaction varies from −20 kJ/mol for CsFAU to −89 kJ/mol for LiFAU. The highest reaction barrier is found for CsFAU (94 kJ/mol) and the lowest for LiFAU (64 kJ/mol).

The isomerization step of **2 → 3** is promoted by the interaction between the migrating O_f and the extraframework cation. Despite this stabilizing interaction, this step is much more difficult than the preceding DAC reaction. The calculated barriers for this step range from 140 kJ/mol for LiFAU to 182 kJ/mol for RbFAU. The next, slightly exothermic, isomerization step (**3 → 4**) to form alcohol **4** proceeds with barriers of 108, 108, 140, 136, and 132 kJ/mol for LiFAU, NaFAU, KFAU, RbFAU, and CsFAU, respectively.

The final dehydration step (**4 → 5**) is strongly exothermic by 104−135 kJ/mol depending on the cation. The reaction is facilitated by the electrostatic stabilization of O_fH by the cation and weak H-bonding interactions with the siliceous framework. Consequently, the activation barrier for the dehydration step (**4 → 5** + H_2O) is rather high. The largest barriers of 188 and 181 kJ/mol are computed for NaFAU and RbFAU, respectively, while the lowest barrier of only 112 kJ/mol is predicted for LiFAU.

The reaction energies and the barriers of the isolated site models (Figure 2a) indicate that the DAC reaction is not the rate-limiting step in the overall reaction sequence. The computed barriers for the isomerization and dehydration steps are much higher than those for the DAC step. These computational results suggest that the catalytic process cannot be achieved under practical conditions. This is in line with the mechanistic proposals put forward by Vlachos and co-workers, who concluded that Brønsted acid catalysis is preferred over Lewis acid catalysis for the dehydration reaction.[22]

This mechanistic picture derived for the MFAU models is very different for the low-silica faujasite model. Figure 2b summarizes the computed reaction energies for the DAC/D reaction of DMF and ethylene over MY models with a Si/Al ratio of 2.4. The supercages of the low-silica faujasite models feature a reactive ensemble consisting of three exchangeable

cations in the proximity of each other, namely, two SII sites and one SIII site. Adsorption of DMF on the SII site is preferred over adsorption on the SIII site because of the enhanced electrostatic stabilization [e.g., $\Delta\Delta E_{ads}^{NaY}$ = −24 kJ/mol (Table S2)]. The starting configuration in **1**/MY involves η^5 coordination of DMF on the SII site and ethylene adsorbed on the opposite SII site (**1**/MY). The adsorption energy for co-adsorption of both reactants in **1**/MY follows the Lewis acidity of the cations; it increases with an increase in Lewis acidity. CsY is an exception from the trend because of the large size of the Cs^+ ion. The possibility of forming more intermolecular contacts with the larger cations in spite of their individual low Lewis acidity leads to an overall stronger adsorption in CsY than in RbY. The DMF···C_2H_4 intermolecular distances gradually decrease with the increasing size of the exchangeable cation (Figure 3a,b). This trend is again broken in the CsY model. Ethylene is displaced because of the large size of the Cs^+
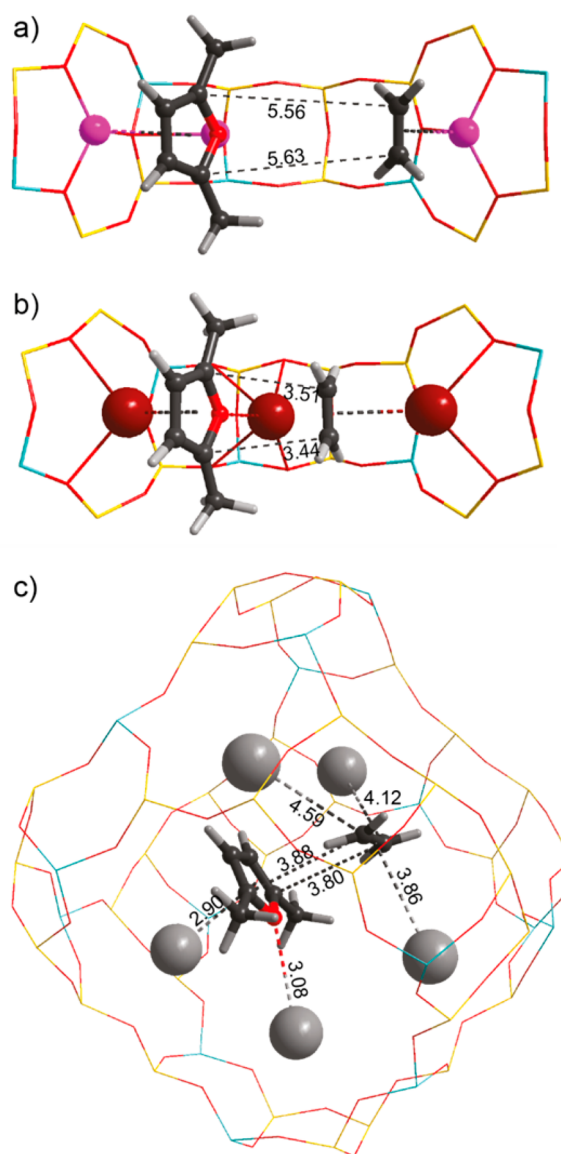
Figure 3. C_{DMF}−$C_{ethylene}$ distances for (a) LiY and (b) RbY. The crowded interior of Cs-exchanged Y is shown in panel c. Color scheme: Si, yellow; Al, blue; O, red; C, dark gray; H, light gray; Cs, light gray; Li, purple; Rb, brown. Optimized distances are given in Ångströms.

ions (Figure 3c). There is not enough space to accommodate both DMF and C_2H_4 between two opposite SII sites, in contrast to all other **1**/MY adsorption geometries.

The **1**/MY co-adsorption complex represents the starting configuration for the DAC reaction. This reaction is most exothermic for RbY (−65 kJ/mol) and least for CsY (−20 kJ/mol). In contrast to the single-site FAU models, the reactivity trend is inverted. For instance, the activation barriers for LiY and NaY are 105 and 107 kJ/mol, respectively, while it is only 62 kJ/mol for RbY. We hypothesize that there can be two explanations for this observation, not necessarily mutually exclusive. The first attributes the trend inversion to electronic structure effects, e.g., sharing of electron density between the two reactants such that an activated complex in **1**/RbY exists. The second is related to the adsorption energy of the individual compounds onto their respective adsorption sites, leading to a higher E_{act} for stronger adsorption. Further detailed electronic structure analysis is required to shed light on the fundamental origin of this phenomenon.

Next, the isomerization steps transform bicyclic intermediate **2** into epoxide **3** and alcohol **4**. The **2** → **3** step is slightly endothermic (16−34 kJ/mol), and the corresponding activation barrier is lowest for LiY and NaY (both 114 kJ/mol), intermediate for KY (143 kJ/mol), and highest for RbY and CsY (158 and 160 kJ/mol, respectively). The second isomerization step, **3** → **4**, is most exothermic for NaY (−59 kJ/mol) and least for CsY (−23 kJ/mol). The lowest barriers of 71 and 67 kJ/mol are computed for LiY and NaY, respectively. KY and RbY promote this step with intermediate barriers of 95 and 86 kJ/mol, respectively, and the highest barrier of 113 kJ/mol is predicted for CsY.

The final product (**5** + H_2O) is obtained in a very exothermic dehydration step. The computed energy changes for this step range from −89 kJ/mol for LiY to −179 kJ/mol for KY. The lowest activation barriers are found for LiY and KY (98 and 80 kJ/mol, respectively) and intermediate barriers for NaY and CsY (117 and 111 kJ/mol, respectively). The highest activation barrier for the dehydration step is found for RbY (167 kJ/mol).

In summary, the presence of multiple accessible active sites in the low-silica model allows for their cooperative action toward confined intermediates and transition states in the catalytic cycle. As a result, the overall computed reaction energetics are altered significantly. The catalyst reactivity trend is changed as compared to those derived from the single-site models; e.g., the DAC reactivity trend is completely inverted. Moreover, the stability of the reaction intermediates increases along the reaction coordinate, leading to lower activation barriers for the isomerization and dehydration barriers.

Isomerization and Dehydration Steps. The results from theoretical studies using the (embedded) cluster approach[21,22] and the current data obtained with periodic DFT calculations on single-site alkali-exchanged MFAU zeolites point to the dehydration step (**4** → **5**) being the rate-limiting step in the DAC/D process. However, in the low-silica MY models, the dehydration barrier is significantly lower. This step is therefore not necessarily rate-limiting in low-silica alkali-exchanged zeolites anymore.

In an attempt to explain the variations in the intrinsic barrier of the dehydration (**4** → **5**) step, we analyzed representative structures of the dehydration transition states: **TS₄**/KFAU and **TS₄**/KY (Figure 4). We focused on the K-exchanged models, because the largest relative decrease in the dehydration activation barrier is observed for KY and because **TS₄**/KY is
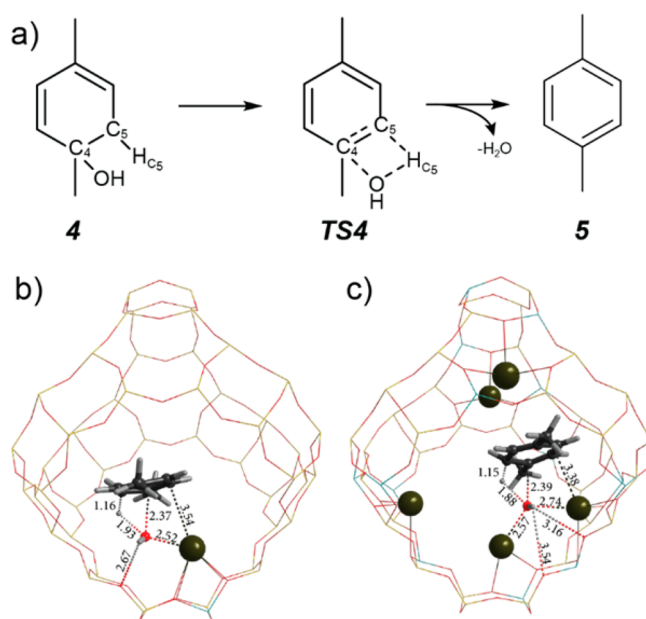

Figure 4. Dehydration of **4** (a) with atom labeling used in the text and respective optimized transition state structures in KFAU (b) and KY (c) models. Selected interatomic distances are given in Ångströms.

more stable than anticipated on the basis of the preceding reaction steps for the MY catalysts (Figure 2b). Two main factors are considered when analyzing the transition states formed in the different models. The first is the increased framework basicity caused by the higher aluminum content of the low-silica MY models.[59] The second is the effect of the exchangeable cations because weaker Lewis acids enhance the basicity of the framework.[60]

The dehydration reaction involves the migration of a C_5-bound proton (H_{C_5}) to a C_4-bound OH moiety of confined alcohol intermediate **4**. In KY, the OH group is in a bridging position between two K^+ ions [$r(HO \cdots K)$ = 2.57 and 2.74 Å], while it coordinates to a single K^+ ion in KFAU [$r(HO \cdots K)$ = 2.52 Å]. These interatomic distances are all within or near the estimated HO $\cdots$ K distance in bulk KOH [$r(HO \cdots K)_{bulk}$ = 2.73 Å].[61] The transition states in KFAU and KY show very similar intermolecular $r(HO \cdots H_{C_5})$ and $r(HO \cdots C_4)$ distances for the activated bonds of the alcohol intermediate (1.93 and 1.88 Å, respectively). The $r(OH^{\delta-} \cdots C_4)$ distances for KFAU and KY are practically the same, i.e., 2.37 and 2.39 Å, respectively. In addition, we expect one significant hydrogen bonding interaction of $OH^{\delta-}$ with the framework in KFAU (2.67 Å), whereas we expect two H-bonds in KY (3.54 and 3.16 Å). Coordination of **TS₄** to SII is also achieved through asymmetric $K^+-\pi_{(C=C)}$ interactions, where SII is located closer to one carbon atom than to the other. The shortest $K^+-C_{C=C}$ distance is 3.54 Å in KFAU and 3.38 Å in KY.

Microkinetic Modeling. Microkinetic modeling was employed to determine the overall reaction rates and compare the performance of the different MY catalysts on the basis of the reaction energy diagrams in Figure 2. The DFT-computed barriers were used to calculate rate constants for the elementary steps in the mechanism. The reaction temperature in the simulations was set to 503 K, and we varied the partial pressures of the reactants. These simulations predict turnover frequencies [TOFs (Figure 5)], reaction orders of DMF and ethylene (Figures S1 and S2, respectively), and active site
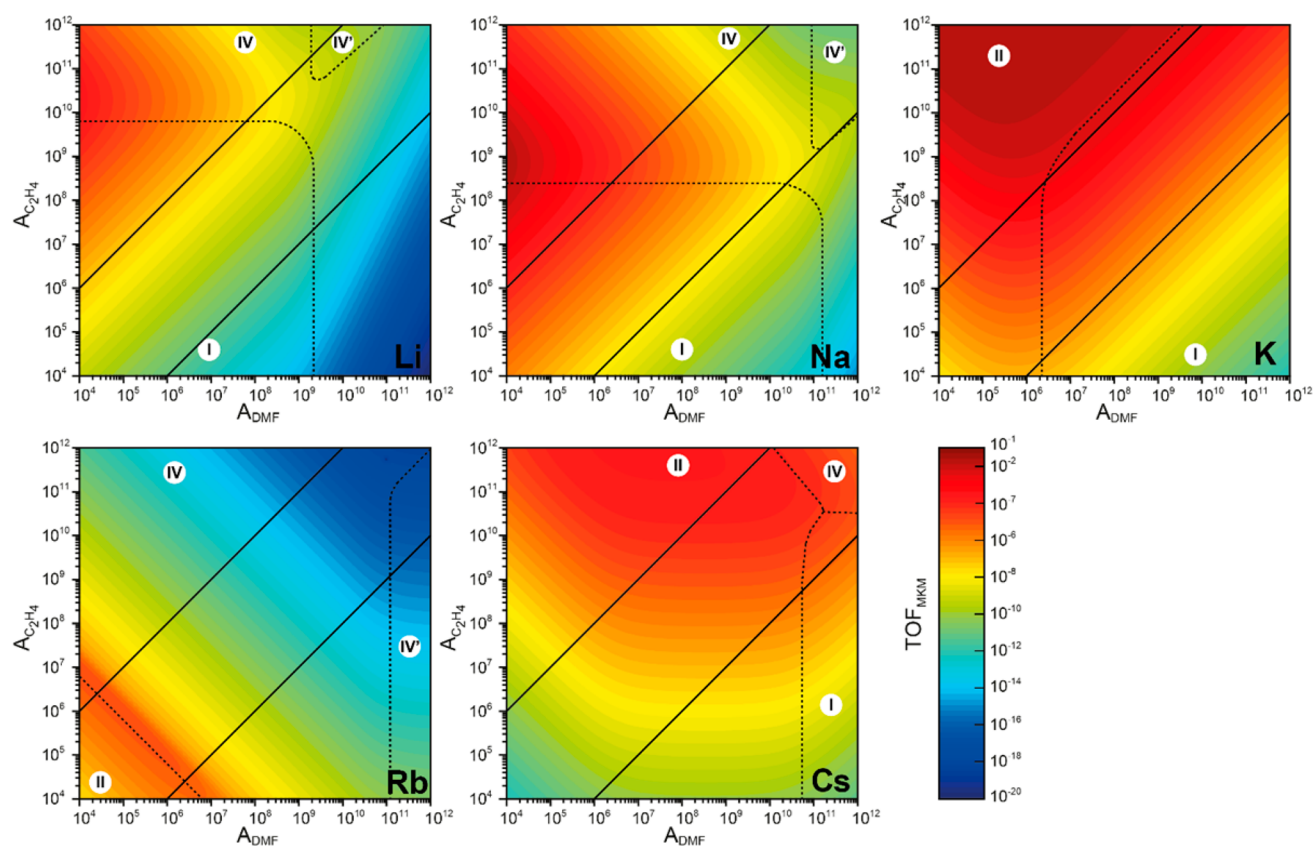
Figure 5. Contour plots of MKM-predicted TOFs as a function of different values of A_{DMF} and $A_{C_2H_4}$ assuming a 1:1 ratio of reactants. The diagonal, solid lines indicate the approximated operating regime of each MY catalyst. The dashed lines indicate the boundaries between the different regimes labeled with Roman numerals. The $1 \rightarrow 2$, $2 \rightarrow 3$, $3 \rightarrow 4$, and $4 \rightarrow 5$ reactions are termed I–IV, respectively. Note that we do not account for gradients in this representation. The prime following the Roman numeral IV indicates that adsorption and desorption of reactants or products are rate-controlling.

coverages by reaction intermediates (Figures S3–S5) as a function of the DMF and C_2H_4 adsorption prefactors (A_{DMF} and $A_{C_2H_4}$, respectively). A DRC analysis is used to identify the most significant rate-controlling and rate-inhibiting elementary reaction steps (Figures S6 and S7).

On the basis of the DRC values, we distinguish four different regimes in which the $1 \rightarrow 2$, $2 \rightarrow 3$, $3 \rightarrow 4$, and $4 \rightarrow 5$ reactions are rate-controlling (regimes I–IV, respectively). A fifth regime is also defined in which the $4 \rightarrow 5$ reaction is rate-controlling while adsorption and desorption of reactants or products are rate-inhibiting (regime IV′). The regimes are indicated in the TOF plot given in Figure 5 in which the rate is given as a function of the adsorption prefactor. The ranges represent variations in the prefactors, which mainly depend on the partial pressure (p_i) and molecular weight ($M_{w,i}$). The region between the solid lines in Figure 5 demarcates the expected experimental regime.

Overall inspection of Figure 5 shows that only three of four potential elementary reaction steps control the rate. These are regimes I, II, and IV in which the $1 \rightarrow 2$ (the DAC reaction), $2 \rightarrow 3$ (the first isomerization), and $3 \rightarrow 4$ (the final dehydration reaction) reactions are rate-controlling. The highest TOFs are found in regime II for KY, RbY, and CsY. Clearly, the highest activity occurs when the first isomerization step controls the overall rate. Regime II does not occur for LiY and NaY under the explored set of conditions.

Consistent with Sabatier's principle, the transition between the regimes is characterized by changes in the reaction orders and the active site coverages. For instance, when going from regime I to IV, the ethylene reaction order changes from +1 to −1, while the DMF reaction order is nearly unaffected. This is in keeping with an increased rate of the DAC reaction with an increased ethylene prefactor, ultimately resulting in a high coverage of the alcohol that needs to be dehydrated in the final step. For large DMF prefactors, we find that both the DAC reaction and the dehydration reaction are significant rate-controlling steps. Of these two elementary reaction steps, the latter controls the rate the most. Furthermore, we note that for large A_{DMF} values and medium to low $A_{C_2H_4}$ values, the adsorption/desorption processes are rate-inhibiting steps. From this analysis, we conclude that the dehydration reaction cannot keep up with either the DAC reaction or DMF adsorption.

Another example consistent with Sabatier's principle is the high TOF observed in regime II for KY, RbY, and CsY. In this regime, approximately half of the available active sites are either vacant or occupied by the DAC reaction product (**2**). Site occupation by **2** is typically found for low values of A_{DMF}. The remaining half of regime II matches with DMF as the most abundant adsorbed species. In addition, the DMF and ethylene reaction orders in regime II both range from zero to approximately +1. At the point of maximum TOF, **2** is the most abundant and DMF and ethylene reaction orders are

positive and close to zero (only for RbY are vacant active sites most abundant at the point of the highest TOF).

From the analysis presented above combined with the TOF contour plots in Figure 5, we conclude that KY, RbY, and CsY are the candidate optimum catalysts. KY is predicted to be the most active one.

Experimental Verification. To verify whether our MKM-based predictions are correct, we synthesized low-silica alkali-exchanged faujasites. They were subjected to kinetic experiments in a batch reactor to determine the initial rates and DMF reaction orders. The measured initial rates and DMF reaction orders are shown in panels a and b of Figure 6, respectively.
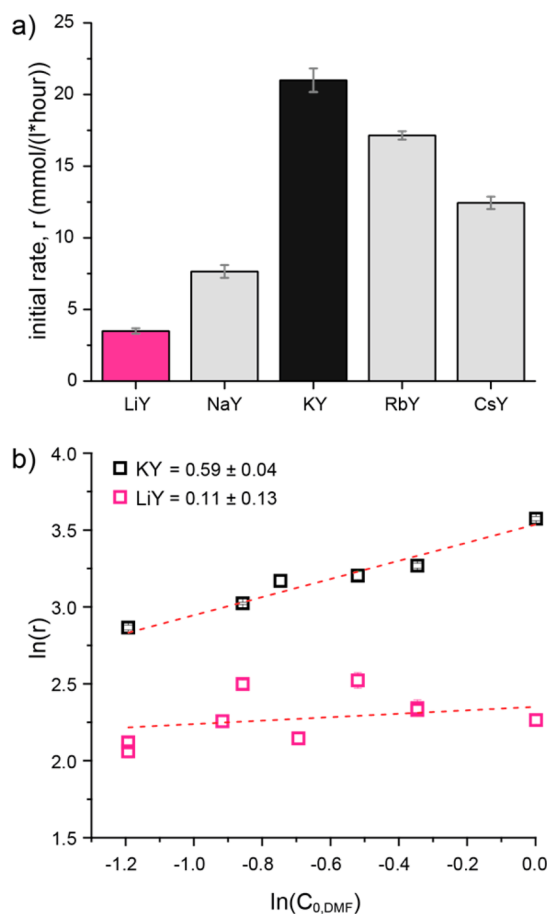
Figure 6. (a) Initial reaction rates of the various alkali-exchanged zeolites tested at 503 K, 60 bar of C_2H_4, and 0.5 M DMF in *n*-heptane. (b) The DMF reaction order is obtained under similar conditions, but with varying DMF concentrations.

Figure S8 shows the fit resulting in Figure 6a. Small-scale blank activity tests (5 mL, batch) showed no conversion of DMF with 20 bar of ethylene in *n*-hexane at 250 °C, indicating the crucial role of the catalyst in the coupling reaction.

The highest initial rate was found for KY (21 mmol L^{-1} h^{-1}). The lowest initial rate was found for LiY (3.5 mmol L^{-1} h^{-1}). DMF reaction orders were also determined for KY and LiY. KY has a positive DMF reaction order of 0.59 ± 0.04, while that for LiY is close to zero (0.11 ± 0.13).

Previous studies report typical reaction rates for the HY catalyst to be in the range of 2−11 mmol L^{-1} h^{-1}.[23] Our data show that the KY catalyst provides an appreciably higher rate of 21 mmol L^{-1} h^{-1} under milder conditions with only 0.5 M

DMF and 230 °C instead of 1.5 M DMF and 250 °C, which were used with the HY catalyst by Vlachos and co-workers.[23] The superior performance of KY is further evidenced by the results of small-scale batch activity tests (see Figure S9). For the alkali-exchanged Y zeolites, the yields of the *p*-xylene product after reaction for 15 h at 250 °C follow the activity trend established by the kinetic experiments (Figure 6). The Brønsted acidic HY catalyst provided a *p*-xylene yield (8%) >2-fold lower than that of KY (21%). In the presence of HY, the 2,5-hexanedione byproduct was formed in an almost equimolar amount (7%), whereas for KY, *p*-xylene was the only identified reaction product.

The exclusive formation of *p*-xylene for the reaction with KY is attributed to the inhibition of the ring-open hydrolysis side reactions due to (i) the use of the nonpolar solvent and (ii) the low Brønsted acidity of the alkali-exchanged zeolite catalysts. Indeed, aliphatic solvents have been shown to enhance *p*-xylene production by reducing the hydrolysis paths to 2,5-hexanedione.[24,62] However, such a promoting solvent effect should be similar for both HY and KY. On the other hand, the ring-opening hydrolysis of DMF is typically catalyzed by strong Brønsted acid sites.[63,64] Such reactions are unlikely to be promoted by the hard extraframework Lewis acid sites or the adjacent basic sites on the lattice in the alkali-exchanged faujasites.

Our results demonstrate that, in contrast to earlier reports,[21] alkali-exchanged faujasites are highly active and selective alternatives to the established HY catalysts for the DAC/D reaction of DMF with ethylene to *p*-xylene. The experiments support the conclusion drawn on the basis of the MKM modeling about the superior activity of KY catalyst, with RbY and CsY being the other two top-performing catalysts. The positive DMF reaction order observed in the experiment is also in agreement with the MKM prediction.

4. CONCLUSIONS

We present a cheap and easy-to-synthesize K-exchanged faujasite zeolite (KY; Si/Al = 2.6) catalyst showing a high activity for the production of *p*-xylene via the one-pot DAC/D reaction of DMF with ethylene. These results allow us to revise earlier conclusions concerning the activity of alkali-exchanged faujasites for this reaction and therefore expand the scope of perspective catalysts well beyond the commonly considered Brønsted acidic systems.

A multiscale computational approach combining periodic DFT calculations with MKM modeling was employed to study the mechanism of the one-pot DAC/D reaction by faujasite-type zeolites. The results of the DFT calculations were directly employed for the construction of a microkinetic model that yielded a catalytic activity trend qualitatively reproduced by our experiments.

The unexpected catalytic performance of the alkali-exchanged faujasites stems from the cooperative nonlinear effects manifested by the complex reactive ensembles involving multiple reactive sites confined within the zeolite microspores. The comparison of the results obtained with the conventional single-site MFAU models with those for the more chemically complex low-silica MY faujasite models points to the importance of the chemically relevant modeling for our mechanistic understanding of these systems. Importantly, the increased chemical complexity of the MY models gave rise to reactivity trends, which could not be predicted from either

classical organic chemistry concepts or the computational results obtained with the reductionist single-site models.

ASSOCIATED CONTENT

⑤ Supporting Information

The Supporting Information is available free of charge on the ACS Publications website at DOI: 10.1021/acscatal.7b03343.

> Details of DFT model definition; DFT-computed DMF and ethylene adsorption energies; supplementary results of microkinetic modeling, including definition of the reaction scheme, DMF and ethylene reaction orders, site occupation, and degree of rate control analysis; and supplementary experimental results, including catalyst characterization data, initial reaction rates, and small-volume batch autoclave experiments (PDF)

AUTHOR INFORMATION

Corresponding Authors
*E-mail: e.j.m.hensen@tue.nl.
*E-mail: e.a.pidko@tudelft.nl.

ORCID
Emiel J. M. Hensen: 0000-0002-9754-2417
Evgeny A. Pidko: 0000-0001-9242-9901

Present Addresses
§I.C.T.: Energy Technology, Department of Mechanical Engineering, Eindhoven University of Technology, P.O. Box 513, 5600 MB Eindhoven, The Netherlands.
∥E.A.P.: Inorganic Systems Engineering group, Department of Chemical Engineering, Faculty of Applied Sciences, Delft University of Technology, Van der Maasweg 9, 2629 HZ Delft, The Netherlands.

Author Contributions
E.U. and B.Z. contributed equally to this work.

Notes
The authors declare no competing financial interest.

ACKNOWLEDGMENTS

REFERENCES

(1) Bukowski, B. C.; Greeley, J. *J. Phys. Chem. C* **2016**, *120*, 6714−6722.
(2) Smit, B.; Maesen, T. L. M. *Nature* **2008**, *451*, 671−678.
(3) Gallego, E. M.; Portilla, M. T.; Paris, C.; León-Escamilla, A.; Boronat, M.; Moliner, M.; Corma, A. *Science* **2017**, *355*, 1051−1054.
(4) Melero, J. A.; Iglesias, J.; Garcia, A. *Energy Environ. Sci.* **2012**, *5*, 7393−7420.
(5) Huber, G. W.; Corma, A. *Angew. Chem., Int. Ed.* **2007**, *46*, 7184−7201.
(6) Zhou, C.-H.; Xia, X.; Lin, C.-X.; Tong, D.-S.; Beltramini, J. *Chem. Soc. Rev.* **2011**, *40*, 5588−5617.
(7) Román-Leshkov, Y.; Davis, M. E. *ACS Catal.* **2011**, *1*, 1566−1580.
(8) Folkins, H. O. In *Ullmann's Encyclopedia of Industrial Chemistry*; Wiley-VCH Verlag GmbH & Co. KGaA: Weinheim, Germany, 2000; Vol. *100C*, pp 41−93.
(9) Fabri, J.; Graeser, U.; Simo, T. A. In *Ullmann's Encyclopedia of Industrial Chemistry*; Wiley-VCH Verlag GmbH & Co. KGaA: Weinheim, Germany, 2000; pp 643−664.
(10) Huber, G. W.; Iborra, S.; Corma, A. *Chem. Rev.* **2006**, *106*, 4044−4098.
(11) Corma, A.; Iborra, S.; Velty, A. *Chem. Rev.* **2007**, *107*, 2411−2502.
(12) Nakagawa, Y.; Tamura, M.; Tomishige, K. *ACS Catal.* **2013**, *3*, 2655−2668.
(13) Besson, M.; Gallezot, P.; Pinel, C. *Chem. Rev.* **2014**, *114*, 1827−1870.
(14) Cheng, Y.-T.; Huber, G. W. *Green Chem.* **2012**, *14*, 3114−3125.
(15) Kappe, C. O.; Murphree, S. S.; Padwa, A. *Tetrahedron* **1997**, *53*, 14179−14233.
(16) Settle, A. E.; Berstis, L.; Rorrer, N. A.; Roman-Leshkóv, Y.; Beckham, G. T.; Richards, R. M.; Vardon, D. R. *Green Chem.* **2017**, *19*, 3468−3492.
(17) Brion, F. *Tetrahedron Lett.* **1982**, *23*, 5299−5302.
(18) Fraile, J. M.; García, J. I.; Gómez, M. A.; de la Hoz, A.; Mayoral, J. A.; Moreno, A.; Prieto, P.; Salvatella, L.; Vázquez, E. *Eur. J. Org. Chem.* **2001**, *2001*, 2891−2899.
(19) Sauer, J.; Sustmann, R. *Angew. Chem., Int. Ed. Engl.* **1980**, *19*, 779−807.
(20) Do, P. T. M.; McAtee, J. R.; Watson, D. A.; Lobo, R. F. *ACS Catal.* **2013**, *3*, 41−46.
(21) Nikbin, N.; Feng, S.; Caratzoulas, S.; Vlachos, D. G. *J. Phys. Chem. C* **2014**, *118*, 24415−24424.
(22) Nikbin, N.; Do, P. T.; Caratzoulas, S.; Lobo, R. F.; Dauenhauer, P. J.; Vlachos, D. G. *J. Catal.* **2013**, *297*, 35−43.
(23) Patet, R. E.; Nikbin, N.; Williams, C. L.; Green, S. K.; Chang, C.-C.; Fan, W.; Caratzoulas, S.; Dauenhauer, P. J.; Vlachos, D. G. *ACS Catal.* **2015**, *5*, 2367−2375.
(24) Williams, C. L.; Chang, C.; Do, P.; Nikbin, N.; Caratzoulas, S.; Vlachos, D. G.; Lobo, R. F.; Fan, W.; Dauenhauer, P. J. *ACS Catal.* **2012**, *2*, 935−939.
(25) Chang, C.; Green, S. K.; Williams, C. L.; Dauenhauer, P. J.; Fan, W. *Green Chem.* **2014**, *16*, 585−588.
(26) Patet, R. E.; Fan, W.; Vlachos, D. G.; Caratzoulas, S. *ChemCatChem* **2017**, *9*, 2523−2535.
(27) Chang, C.-C.; Je Cho, H.; Yu, J.; Gorte, R. J.; Gulbinski, J.; Dauenhauer, P.; Fan, W. *Green Chem.* **2016**, *18*, 1368−1376.
(28) Wijaya, Y. P.; Suh, D. J.; Jae, J. *Catal. Commun.* **2015**, *70*, 12−16.
(29) Li, Y. P.; Head-Gordon, M.; Bell, A. T. *ACS Catal.* **2016**, *6*, 5052−5061.
(30) Pacheco, J. J.; Davis, M. E. *Proc. Natl. Acad. Sci. U. S. A.* **2014**, *111*, 8363−8367.
(31) Pacheco, J. J.; Labinger, J. A.; Sessions, A. L.; Davis, M. E. *ACS Catal.* **2015**, *5*, 5904−5913.
(32) Shiramizu, M.; Toste, F. D. *Chem. - Eur. J.* **2011**, *17*, 12452−12457.
(33) Ni, L.; Xin, J.; Dong, H.; Lu, X.; Liu, X.; Zhang, S. *ChemSusChem* **2017**, *10*, 2394−2401.
(34) Teixeira, I. F.; Lo, B. T. W.; Kostetskyy, P.; Stamatakis, M.; Ye, L.; Tang, C. C.; Mpourmpakis, G.; Tsang, S. C. E. *Angew. Chem., Int. Ed.* **2016**, *55*, 13061−13066.
(35) Pidko, E. A. *ACS Catal.* **2017**, *7*, 4230−4234.
(36) Stamatakis, M.; Vlachos, D. G. *ACS Catal.* **2012**, *2*, 2648−2663.
(37) Chizallet, C.; Raybaud, P. *Catal. Sci. Technol.* **2014**, *4*, 2797−2813.
(38) López, N.; Almora-Barrios, N.; Carchini, G.; Błoński, P.; Bellarosa, L.; García-Muelas, R.; Novell-Leruth, G.; García-Mota, M. *Catal. Sci. Technol.* **2012**, *2*, 2405−2417.
(39) Ahlquist, M.; Periana, R. A.; Goddard, W. A., III *Chem. Commun.* **2009**, *0*, 2373−2375.
(40) Krauter, C. M.; Hashmi, A. S. K.; Pernpointner, M. *ChemCatChem* **2010**, *2*, 1226−1230.

(41) Siegbahn, P. E. M. *Q. Rev. Biophys.* **2003**, *36*, 91−145.

(42) Warshel, A. *Annu. Rev. Biophys. Biomol. Struct.* **2003**, *32*, 425−443.

(43) Pidko, E. A.; Mignon, P.; Geerlings, P.; Schoonheydt, R. A.; Van Santen, R. A. *J. Phys. Chem. C* **2008**, *112*, 5510−5519.

(44) Pidko, E. A.; Van Santen, R. A. *Int. J. Quantum Chem.* **2010**, *110*, 210−220.

(45) Kresse, G.; Hafner, J. *Phys. Rev. B: Condens. Matter Mater. Phys.* **1994**, *49*, 14251−14269.

(46) Kresse, G.; Furthmüller, J. *Phys. Rev. B: Condens. Matter Mater. Phys.* **1996**, *54*, 11169−11186.

(47) Kresse, G.; Furthmüller, J. *Comput. Mater. Sci.* **1996**, *6*, 15−50.

(48) Kresse, G.; Joubert, D. *Phys. Rev. B: Condens. Matter Mater. Phys.* **1999**, *59*, 1758−1775.

(49) Kresse, G.; Hafner, J. *Phys. Rev. B: Condens. Matter Mater. Phys.* **1993**, *47*, 558−561.

(50) Grimme, S.; Antony, J.; Ehrlich, S.; Krieg, H. *J. Chem. Phys.* **2010**, *132*, 154104.

(51) Grimme, S.; Ehrlich, S.; Goerigk, L. *J. Comput. Chem.* **2011**, *32*, 1456−1465.

(52) Henkelman, G.; Uberuaga, B. P.; Jónsson, H. *J. Chem. Phys.* **2000**, *113*, 9901−9904.

(53) Henkelman, G.; Jónsson, H. *J. Chem. Phys.* **2000**, *113*, 9978−9985.

(54) Filot, I. A. W.; Zijlstra, B.; Hensen, E. J. M. *MKMCXX, a C++ program for constructing microkinetic models*; http://www.mkmcxx.nl.

(55) Filot, I. A. W.; Van Santen, R. A.; Hensen, E. J. M. *Angew. Chem., Int. Ed.* **2014**, *53*, 12746−12750.

(56) Hänggi, P.; Talkner, P.; Borkovec, M. *Rev. Mod. Phys.* **1990**, *62*, 251−341.

(57) Eyring, H. *Chem. Rev.* **1935**, *17*, 65−77.

(58) Stegelmann, C.; Andreasen, A.; Campbell, C. T. *J. Am. Chem. Soc.* **2009**, *131*, 8077−8082.

(59) Schoonheydt, R. A.; Geerlings, P.; Pidko, E. A.; Van Santen, R. A. *J. Mater. Chem.* **2012**, *22*, 18705−18717.

(60) Walton, K. S.; Abney, M. B.; LeVan, M. D. *Microporous Mesoporous Mater.* **2006**, *91*, 78−84.

(61) Shannon, R. D. *Acta Crystallogr., Sect. A: Cryst. Phys., Diffr., Theor. Gen. Crystallogr.* **1976**, *32*, 751−767.

(62) Xiong, R.; Sandler, S. I.; Vlachos, D. G.; Dauenhauer, P. J. *Green Chem.* **2014**, *16*, 4086−4091.

(63) Gubina, T. I.; Labunskaya, V. I.; Kornienko, G. K.; Borodina, L. A.; Kharchenko, V. G. *Chem. Heterocycl. Compd.* **1995**, *31*, 548−552.

(64) Piancatelli, G.; D'Auria, M.; D'Onofrio, F. *Synthesis* **1994**, *1994*, 867−889.